



## Additive manufacturing of functionally graded foams for acoustic insulation and absorption



Prasansha Rastogi, Cornelis H. Venner, Claas Willem Visser\*, Ysbrand Wijnant\*

*Engineering Fluid Dynamics Group, Department of Thermal and Fluid Engineering, Faculty of Engineering Technology, University of Twente, P.O. Box 217, 7500 AE, Enschede, the Netherlands*

### ABSTRACT

Acoustic foams and foam-filled metamaterials excel at sound absorption but typically exhibit a low sound transmission loss (STL). Foams that precisely integrate tunable shapes, density gradients, and transitions between open-cell and closed-cell regions have the potential to simultaneously enhance absorption and STL as compared to uniform foams. However, fabrication of these materials is challenging even for small samples that consist of a few thousand unit cells. Here we show additive manufacturing of functionally graded foams via *direct bubble writing*, a method for generating and stacking bubbles into three-dimensional solid foam constructs with a throughput up to 100 ml/min. The density, pore morphology, flow resistivity, and dynamic mechanical behavior of homogeneous and graded foams are characterized. As a reference case, the STL and absorption of homogeneous samples were tested in an impedance tube for frequencies between 200 Hz and 2600 Hz. Graded samples were subsequently evaluated, revealing strongly enhanced peaks in STL (up to ~68 dB) for closed-cell foams with a low-density core sandwiched between two high-density layers. A high-density core sandwiched between two low-density layers especially broadens the frequency range with high sound absorption and still enhances the STL. These results show that functionally graded closed-cell foams are a promising route towards structure-induced dissipation as required for materials that exhibit a high absorption and a high STL.

### 1. Introduction

Within Europe, up to 67 % of the urban population is exposed to road traffic noise, leading to adverse effects including cognitive and cardiovascular health and hearing loss [1–4]. Reducing noise requires innovative materials (1) for preventing transmission of sound into e.g. buildings, and (2) for preventing reflections of sound from hard surfaces. Materials optimized for transmission loss are thick or dense, and traditionally consist of metal plates, bricks, or concrete. However, application of these heavy materials results in surface reflections that increase e.g. roadside noise [5,6] and their applicability in e.g. aerospace is limited. In contrast, porous materials with a lower density, such as foams or acoustic metamaterials, absorb sound very well but exhibit a low STL. For example, the acoustic absorption of foams was optimized as a function of the density, the pore size, and the open-cell fraction [7–11]. Graded porous materials further improved absorption at low frequencies [12].

Porous materials that integrate absorption and a high STL were recently investigated, as these are desirable for a range of applications. Slag-based inorganic foams [13], aluminum foams, and melamine foams resulted in limited improvements of the STL as compared to the bulk material. However, introducing porosity enhanced the STL of rubber by

14 dB, and of polyurethane up to 30 dB for frequencies below 2000 Hz [14–19]. In graded foams, each layer exhibits a different shape of the cells (circular or elliptical), a different porosity type (open or closed), or a different cell size (tortuosity). Such gradients enhance the dissipation and thereby the STL [12,20–24]. Similarly, porous materials that incorporated four different cell sizes (between 1 mm and 4 mm) improved the STL compared to their uniform counterparts by 2.5 dB to 15 dB [12]. However, controlling the microstructure of functionally graded porous materials remains an enormous challenge, which consists of (1) controlling the porosity, the cell size, and the interconnectivity between pores of a homogeneous foam and (2) the ability to create gradients in any of these properties [25,26]. One strategy to create gradients is adapting traditional materials, for example by gluing pieces with different properties or by precise control of temperatures or blowing agents during foaming [20,27–31]. Here, samples of a substantial size can be fabricated, but the properties of the unit cells exhibit a broad distribution. Alternatively, additive manufacturing (AM) provides precise control over the architecture of the cellular materials. However, it does not easily incorporate closed cells as desired for materials with a high STL [12,32] and AM has a low throughput, as each cell is generally built layer-by-layer.

Here we leverage *direct bubble writing* (DBW) [33] as an additive

\* Corresponding authors.

E-mail addresses: [c.visser@utwente.nl](mailto:c.visser@utwente.nl) (C.W. Visser), [y.h.wijnant@utwente.nl](mailto:y.h.wijnant@utwente.nl) (Y. Wijnant).

manufacturing platform for foams with locally tunable density gradients, controlled open-to-closed cell transitions, and a high throughput of up to 100 mL/min. Uniform and graded samples are printed and their acoustic performance is systematically evaluated. Section 2 describes the methods for printing sandwich-inspired foams and for the acoustic measurements. Section 3 discusses the acoustic performance of the uniform and gradient foams and their mechanical, morphological, and optical characterizations. The discussion and the conclusions are presented in sections 4 and 5, respectively.

## 2. Materials and methods

### 2.1. Materials

All chemicals, poly (ethylene glycol) diacrylate (PEGDA) (molecular weight 700 g/mol (number-averaged)), diphenyl(2,4,6-trimethylbenzoyl)phosphine oxide (TPO), and Tween 20 (a polysorbate-based non-ionic surfactant) were obtained from Sigma-Aldrich, Germany. Demineralized (DM) water was used for all ink formulations.

### 2.2. Ink preparation

The base formulation of the ink consisted of a 1:1 ratio of PEGDA in DM water. 2 wt% Tween 20 (with respect to the PEGDA:DM water mixture) was added as a bubble stabilizer to the base formulation. 1 wt% of TPO (with respect to the pure PEGDA in the PEGDA:DM water mixture) was added to aid the ink curing. The ink mixture was stirred overnight using a magnet in a closed container until a clear homogeneous ink was observed. Before using the ink for printing, it was nitrogen-purged for 15 min to eliminate traces of oxygen that could inhibit acrylate polymerization. The ink was prepared and used for printing in a lab with yellow lighting, preventing premature polymerization due to blue or green light exposure under standard lighting conditions.

### 2.3. Printer layout and operation

The heart of the setup is a core-shell nozzle that ejects the PEGDA ink through the shell of the nozzle and a gas through the core nozzle, as shown in Fig. 1 (a). The ink flow rate was set to  $Q = 15 \text{ ml/min}$  unless

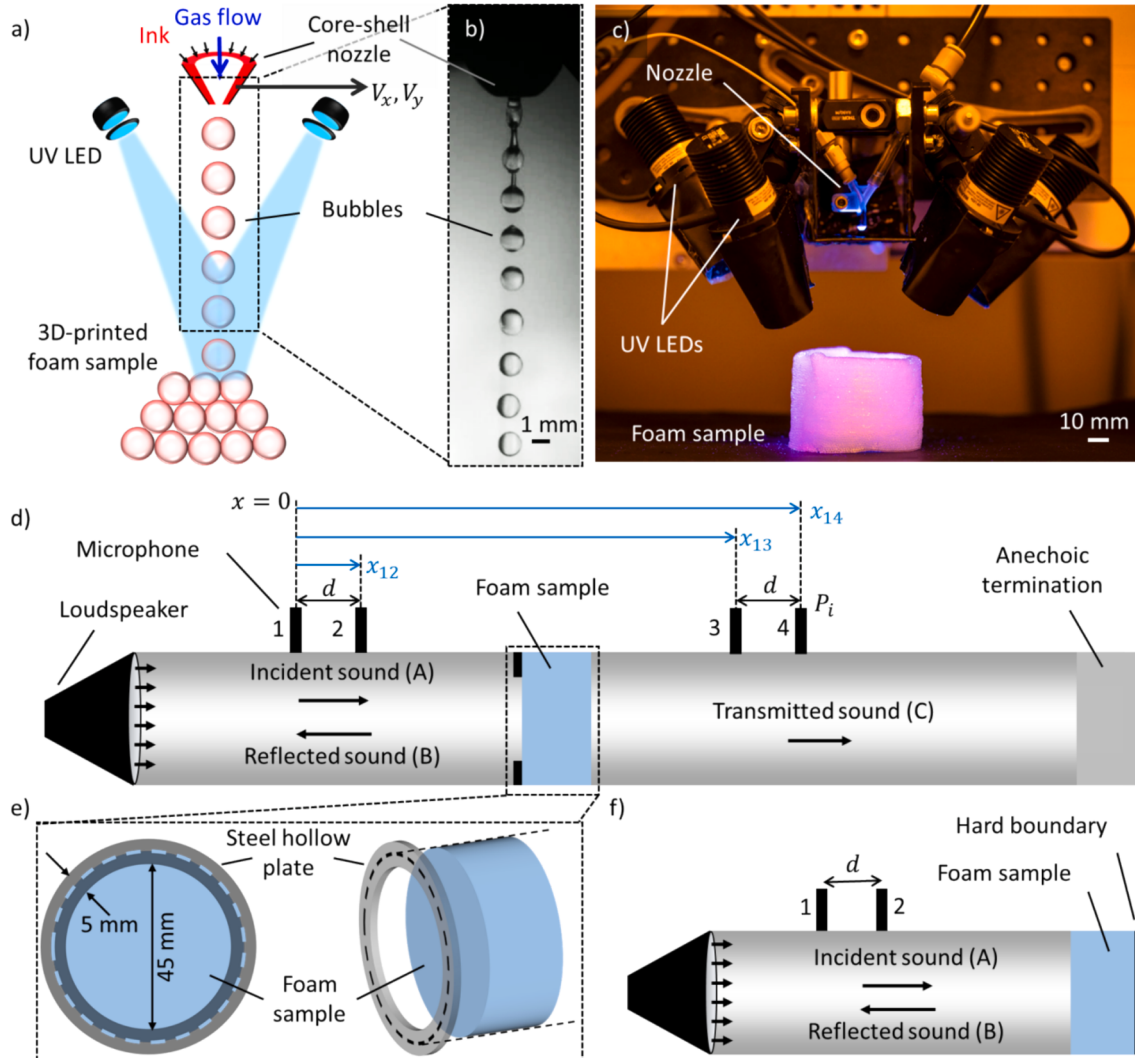


**Fig. 1.** Overview of the foam printing process and the impedance tube. a) Foams are printed by ejecting a gas through the core of a coaxial nozzle and a liquid monomer-containing ink through its shell. The nozzle motion follows a prescribed print path with velocity  $V_x, V_y$  as indicated by the arrow, yielding a 3D printed foam. Bubbles are formed at the tip of the nozzle, which are polymerized on-the-fly and fully cured after impact. b) Photograph of the bubble train, for  $P = 7.5 \text{ kPa}$ . The nozzle is visible at the top (black; an image of the nozzle is shown in Fig. SI 1). c) Photograph of the printhead, including a finished foam sample. d) Impedance tube for measuring the transmission loss of foam samples. The foams are mounted behind a ring with a width of 5 mm (figure e) to prevent sound leakage. f) The acoustic absorption is measured by implementing a hard boundary behind the foam as the termination of the impedance tube.

otherwise reported. The nozzle generates a continuous stream of bubbles (Fig. 1 (b)) in the air that flies downwards for approximately 10 cm until it hits the build platform. The nozzle (Fig. SI 1(b)) is mounted on a printhead as shown in Fig. 1 (c). During printing, the stream of ejected bubbles is exposed to UV light emitted from four directions, by two LEDs emitting at a wavelength of 365 nm and two LEDs emitting at a wavelength of 370 nm (Thorlabs, Germany). The LEDs illuminate a section of the bubble stream and a circular spot on the build platform with a diameter of  $70 \pm 10$  mm, resulting in photo-polymerization of bubbles before and during impact.

A central computer controls the motion of the printhead in the  $x-y-z$  plane as well as the ink and the gas flows. A camera records the bubble ejection, as shown in Fig. SI 1 (a). The print path is prescribed by Motion Perfect software (Trio Motion Technology, United Kingdom). The printed filaments usually have a shape that is virtually equal to the trajectory of the nozzle. Any discrepancies between the nozzle path and the shape of printed foams are discussed in ref. [34]. Printing multiple layers then yields the 3D-printed foam samples.

Cylinder-shaped foam samples with a typical diameter of 60 mm and a height between 5 mm and 70 mm were printed layer by layer. The printhead followed a spiral-shaped print path which was repeated several times, each instance resulting in one foam layer. Homogeneous foam samples were printed by applying a constant gas pressure during printing. Foams with density gradients were produced by tuning the gas pressure from 5.5 kPa to 8.5 kPa during printing. The gas pressure adjustment induced a transition from high-density ( $\rho = 250 \text{ kg/m}^3$ ) to low-density ( $\rho = 125 \text{ kg/m}^3$ ), and vice-versa. The thickness of each high- or low-density section was set by adjusting the number of printed foam layers. Printing a typical 4 layer foam sample with a volume of 33  $\text{cm}^3$  (and a density  $\rho = 150 \text{ kg/m}^3$ ) resulted in a printing time of only ~35 sec.

After printing, the foam samples were manually removed from the platform and flooded with UV light (365 nm) for 2 min to polymerize any uncured PEGDA. These samples were then left to dry for 50 days to evaporate any water from the cured resin. This long drying time is a bottleneck of solvent-containing resins (here, the solvent is water). During the drying process, the water diffuses out, causing the polymer foam to shrink. Therefore, drying is required to obtain shape-stable stable samples. Gentle drying is required to prevent stress-induced cracking of the dried parts of the foam. Hence, resolving this issue would require a transition to solvent-free foams, which we recently achieved for foams with a higher relative density [35].

#### 2.4. Density characterization

Printed foams were cropped into a cylindrical cross-sectional geometry by using a circular 50 mm diameter die hole punch. Dimensions and mass of the foams were measured using vernier calipers and a weighing scale, respectively. The density,  $\rho_f$ , of the foams was determined from these parameters. The relative density is defined as  $\rho_f/\rho_b$ , with  $\rho_b = 1060 \text{ kg/m}^3$  the density of the polymerized non-porous PEGDA ink.

#### 2.5. Structural characterization

Micro-computed tomography (micro-CT, Zeiss Xradia Context Micro-CT, Germany) was used to investigate the three-dimensional internal morphology of the printed foams, resulting in grayscale color contrasts. Cuboid foam samples with a size of 10 mm\*10 mm\*15 mm were scanned with a pixel size between 6.6  $\mu\text{m}$  and 17  $\mu\text{m}$ . A 3D view of the sample was acquired by rotating the sample 360° with a step rotation angle of 0.08°. After complete scanning, all the projections were reconstructed in software (Scout and Scan Control System Reconstructor). Dragonfly and 3D slicer software were used to visualize the internal 3D microstructural features. The voltage of the X-rays was set to 60 kV and the

radiation power to 5 W. The scanned tomograms were post-processed using a home-made Python script that provided the void fraction based on the micro-CT scans.

#### 2.6. Acoustic characterization

The acoustic transmission of the foams was determined in an impedance tube with an internal diameter of 50 mm, 4-microphone setup, and an anechoic sound termination, as shown in Fig. 1 (d) and Fig. SI 4. Both the absorption and the sound transmission loss (STL) of the foam samples were measured for a frequency sweep from 200 Hz to 2600 Hz. The measurements were analyzed with a 1 Hz resolution.

The setup consists of a power amplifier (Type 2706, Brüel & Kjaer, Denmark) which amplifies the sound signal sent to the loudspeaker. The emitted sound travels as a plane wave inside the hollow aluminum impedance tube. The frequency range between 200 Hz to 2600 Hz is used to ensure plane-wave propagation. The 4 highly sensitive microphones (Microtech Gefell GmbH, Germany) as indicated in Fig. 1 (d) are used to record the pressure fluctuations on the incident and transmitted side of the sample. Each pair of microphones 1–2 and 3–4 is equally separated at a distance  $d = 38$  mm. To prevent unwanted sound leakage between the edge of the sample and the impedance tube, the sample is mounted as shown in Fig. 1 (e). The mount consists of a 2 mm thick steel circular ring with an outer diameter of 50 mm and an inner diameter of 45 mm, covering 2.5 mm of the edge of the foam. The transmitted sound is detected by microphones 3 and 4 providing a quantitative measurement of the sound transmission loss of the printed foams after processing. The anechoic termination of the tube is provided by melamine foam with a diameter of 50 mm and thickness of 300 mm.

Microphones 1 and 2 record a pressure  $P_m = Ae^{(-1)^m i k x_{1m}} + Be^{(-1)^{m+1} i k x_{1m}}$ , and microphones 3 and 4 record a pressure  $P_n = Ce^{(-1)^n i k x_{1n}} + De^{(-1)^{n+1} i k x_{1n}}$ . Here,  $m = [1, 2]$  and  $n = [3, 4]$  denote the respective microphones as shown in Fig. 1 (d),  $P$  denotes the (complex) amplitude of the Fourier transformed time signal (hence  $P$  denotes the amplitude at a given frequency),  $x_{1m}$  is the distance from the microphone 1 to microphone  $m$ , and  $k = \frac{2\pi f}{c}$  denotes the wave number with  $f$  the frequency and  $c$  the speed of sound in air.  $A, B, C$ , and  $D$  represent the complex amplitudes for the incident sound from the loudspeaker, the reflected sound from the sample, the transmitted sound through the sample, and the reflected sound pressure from the tube termination, respectively.

The pressure signals from the microphones are post-processed in Matlab to determine the complex pressure amplitudes, A–D, and the STL. The amplitudes are extracted from the above equations as:

$$A = \frac{i(P_1 e^{ikx_{12}} - P_2 e^{ikx_{11}})}{2\sin(k(x_{11} - x_{12}))} \quad (1)$$

$$B = \frac{i(-P_1 e^{-ikx_{12}} + P_2 e^{-ikx_{11}})}{2\sin(k(x_{11} - x_{12}))} \quad (2)$$

$$C = \frac{i(P_3 e^{ikx_{14}} - P_4 e^{ikx_{13}})}{2\sin(k(x_{13} - x_{14}))} \quad (3)$$

$$D = \frac{i(-P_3 e^{-ikx_{14}} + P_4 e^{-ikx_{13}})}{2\sin(k(x_{13} - x_{14}))} \quad (4)$$

We define  $x_{11} = 0$  at microphone 1 and  $D = 0$  due to anechoic termination.

The sound transmission ( $\tau$ ) and the sound transmission loss (STL) are defined by equations (5) and (6):

$$\tau = \frac{C^* \bar{C}}{A^* \bar{A}} \quad (5)$$

$$STL = -10\log_{10}(\tau) \quad (6)$$

where  $\bar{A}$  denotes the complex conjugate of  $A$ .

The sound absorption of the foam samples was measured by placing a 5 mm thick aluminum plate, acting as a hard boundary, directly behind the sample, as shown in Fig. 1 (f). The reflection coefficient ( $r$ ) and the sound absorption coefficient ( $\alpha$ ) are given by equations (7) and (8):

$$r = \frac{B^* \bar{B}}{A^* \bar{A}} \quad (7)$$

$$\alpha = 1 - r \quad (8)$$

Finally, the dissipation ( $\delta$ ) was readily determined as:  $\delta = 1 - \tau - r$ , assuming all sound energy impinging on the sample is either reflected, transmitted, or dissipated by the sample. All measurements for the STL and the absorption were repeated at least 4 times, averaged, and plotted as shown in Figs. 3–5.

Sandwich-type foams were printed with density gradients in stiff-soft-stiff (4-4-4 layers) and in soft-stiff-soft (4-4-4 layers) configurations. Three samples were printed for each of these configurations. The STL and absorption of these samples were measured and compared to evaluate potential sample-to-sample differences (Fig. SI 7). The stiff and soft sections represented the high- and the low-density printed parts in a gradient foam sample, respectively. One sample of each uniform and

gradient (stiff-soft-stiff) density foams was characterized via micro-CT scanning, as shown in Fig. SI 2 and Fig. SI 3. The average and the standard deviation of the measured values of the STL and absorption are shown in Fig. SI 7. A uniform sample and the gradient samples were also tested for STL and absorption on three different days, as shown in Fig. SI 8. Some degradation was observed, possibly due to breaking of pore shells in the low-density center section as the samples were slightly compressed during mounting. These and other samples were also measured multiple times, as described above and discussed in the main text.

## 2.7. Mechanical characterization

Cuboidal foam samples with cross-section of 10 mm\*10 mm were tested using dynamic mechanical analysis (DMA, Eplexor instrument 2000 N, Netzsch, Germany). Dynamic testing of all the samples was performed in compression mode at a fixed temperature of  $20 \pm 2^\circ\text{C}$ . The frequency was varied from 1 Hz to 100 Hz in 41 logarithmically-distributed points. This frequency sweep started when the contact force reached 0.4 N, ensuring complete cross-sectional contact of the foam with the compressing plate. The foam samples were compressed at a speed of 40 mm/min undertaking static strain of 0.2 % and dynamic strain of 0.1 %. A load cell of 500 N was used during all the experiments

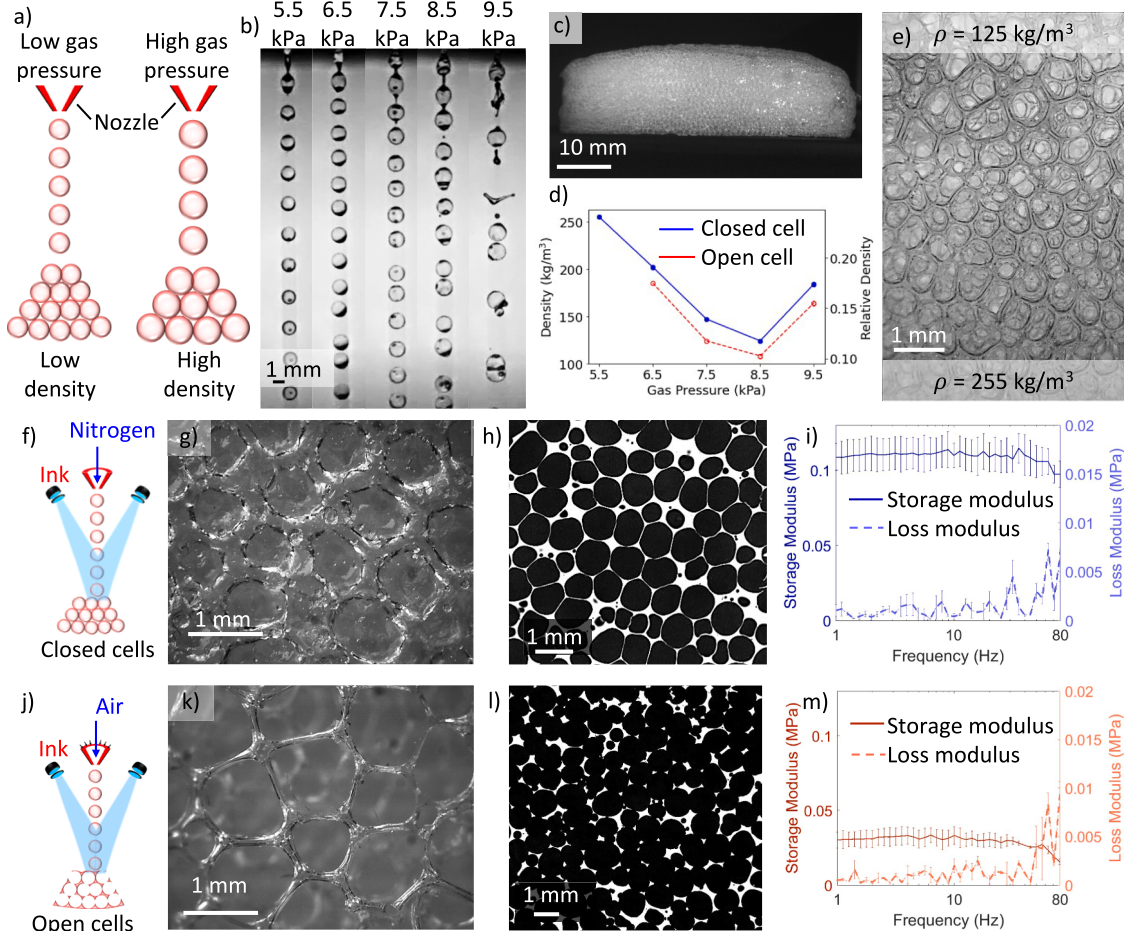


**Fig. 2.** Fabrication and characterization of printed foam samples. a) Increasing the gas pressure applied to the nozzle leads to a higher relative air volume in the foam. b) High-speed images of the ejected bubble stream as a function of the gas pressure. c) Side-view of a foam sample printed with a gas pressure of 7.5 kPa. d) The measured density as a function of the gas pressure, for open- and closed-cell foams. e) Optical microscopy image of a gradient foam sample. Here, the gas pressure was increased from 5.5 kPa to 8.5 kPa to print sections with  $\rho = 255 \text{ kg/m}^3$  and  $\rho = 125 \text{ kg/m}^3$ , respectively. f) Printing with nitrogen gas results in closed-cell foams as characterized (g) by an optical microscope and (h) by micro-CT scanning. In micro-CT scanned images, the white regions depict the solid PEGDA and the black color indicates gas. i) The storage and loss moduli as measured for this sample. j) For air-filled foams, diffusive penetration of oxygen into the cell walls prevents solidification. Only the thicker struts solidify, yielding open cell foams as characterized k) by optical microscopy, l) by micro-CT scanning, and m) by mechanical testing.

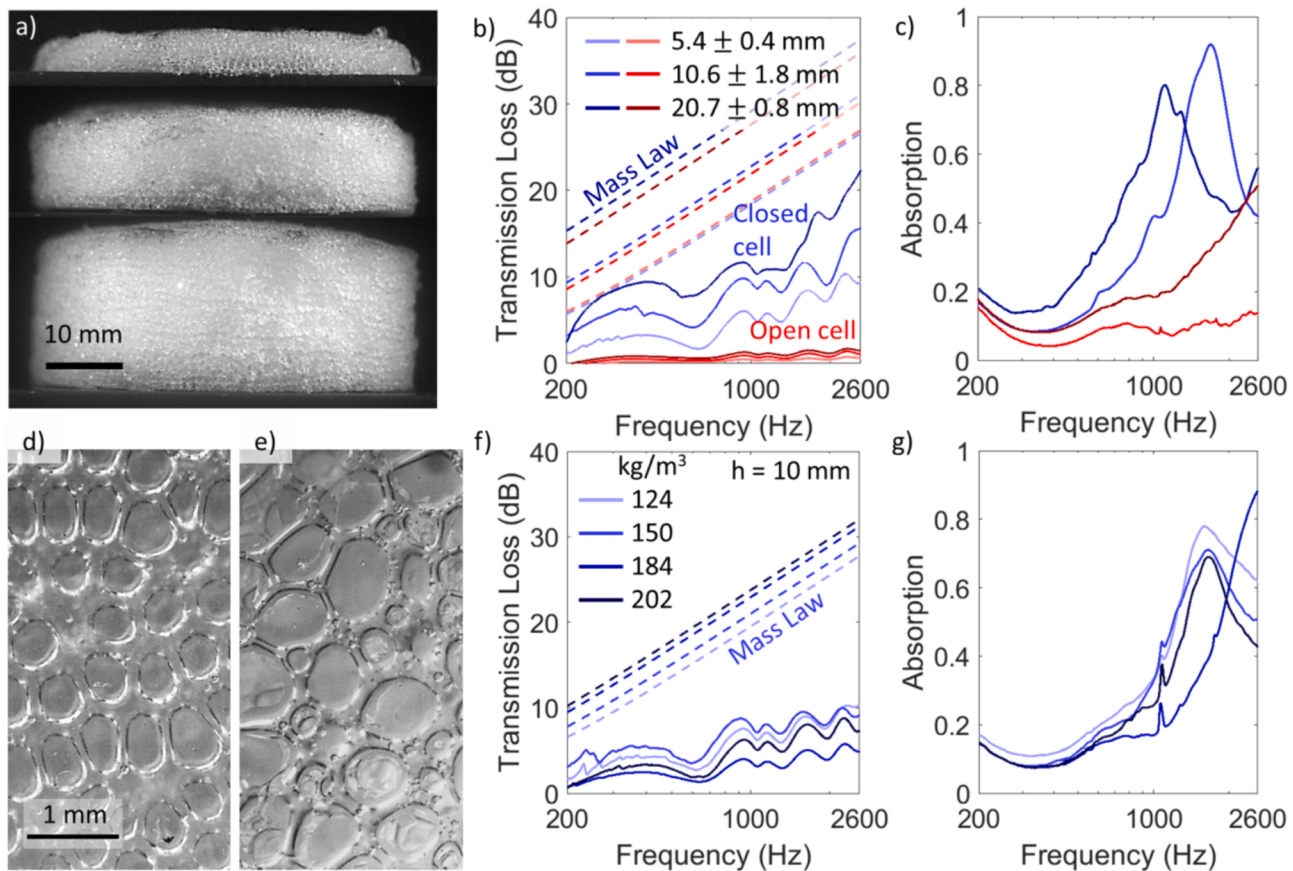


**Fig. 3.** Acoustic characterization of homogeneous foams. a) Side view of samples of increasing thickness, printed with a nitrogen pressure 7.5 kPa. From top to bottom, samples consisting of [2,4,8] printed layers are shown. b) Sound transmission loss and c) sound absorption for closed-cell and open-cell samples as a function of the thickness. The dashed lines indicate the sound transmission loss predicted by the mass law. d) Optical microscopy image of closed-cell foams printed at  $P = 6.5$  kPa ( $\rho = 202 \text{ kg/m}^3$ ) and e) 8.5 kPa ( $\rho = 124 \text{ kg/m}^3$ ). f) Sound transmission loss and g) sound absorption for closed-cell foams of different densities.

under compression. Three test specimens of each category were tested for computing the storage ( $E'$ ) and loss ( $E''$ ) modulus and the loss factor ( $\tan\delta_{LF}$ ). To determine the behavior of sample in the acoustic frequency range of 200 Hz to 2600 Hz, a master curve was plotted using the time-temperature superposition principle [36]. Here, the temperature was increased in steps of 5 °C from -20 °C to -5 °C during the frequency sweep. After each temperature increment, the sample was thermally equilibrated for 5 min before subsequent dynamic testing.

### 3. Results

The production of bubbles from the core-shell nozzle was controlled by the ink flow rate and the gas pressure applied to the nozzle, as shown in Fig. 1 (a). We assessed the influence of the pressure on the continuous production of bubbles as shown in Fig. 2 (a, b). By increasing the gas pressure from  $P = 5.5$  kPa to 8.5 kPa, more gas was enclosed by each bubble and the frequency of bubble ejection from the nozzle also increased. In this regime, samples were readily printed, as shown in Fig. 2 (c) for  $P = 7.5$  kPa. The lowest density  $\rho = 125 \text{ kg/m}^3$  was reached for  $P = 8.5$  kPa, corresponding to  $\rho_{rel} = 0.12$  as shown in Fig. 2 (d). Further increasing the gas pressure to  $P = 9.5$  kPa resulted in bursting of bubbles, increasing the density of the foam [33]. Fig. 2 (e) shows an example of a density gradient foam that was printed at gas pressures of 5.5 kPa and 8.5 kPa. The structure of this foam was characterized by micro-CT scanning, as shown in Fig. SI S2 and Fig. SI S3 (g, h, i).

A transition from closed-cell to open-cell foams was achieved by switching the gas type to fill the bubbles from nitrogen to air [33]. Closed-cell foams are formed when the entire bubble is solidified, which

is observed if nitrogen is used. The underlying mechanism is that the photoinitiator dissociates into active radicals under UV irradiation, which react with monomer double bonds and thereby form the polymer chains. Nitrogen is unreactive with the acrylate radicals in the ink and therefore the bubbles polymerize entirely when exposed to UV light [37,38] (Fig. 2 (f)). However, in presence of oxygen, peroxy radicals are formed which deplete the active radicals and terminate the photopolymerization reaction. As the faces between the cells are thinner than the oxygen penetration depth by diffusion into the still-liquid resin (see [33] for details), polymerization is blocked and the faces do not polymerize. In contrast, the struts are thicker than the oxygen diffusion depth at the time of polymerization. Hence the struts polymerize and form an open-cell foam [39–41].

A closed-cell foam printed at 7.5 kPa was visualized with optical microscopy as shown in Fig. 2 (g). Micro-CT scanning confirmed the closed-cell structure as shown in Fig. 2 (h) and Fig. SI 3 (d, e, f), and revealed  $\sim 50\mu\text{m}$  thick walls that separated the adjacent pores. The storage modulus of the closed-cell foam was measured to be  $0.11 \pm 0.01$  MPa, as shown in Fig. 2 (i). However, when air was used, foams with open cells were produced as shown in Fig. 2 (j, k) and Fig. SI 3 (a, b, c) [42]. The cross section was determined using micro-CT, as shown in Fig. 2 (l). The cell size was determined to be  $895 \pm 50\mu\text{m}$  and the storage modulus was measured to be  $0.03 \pm 0.01$  MPa (Fig. 2 (m)). Open-cell foams were softer than their closed-cell counterparts because the faces of closed cells strongly resist deformation [43,44]. Therefore, controlling the gas type in direct bubble writing controls both the stiffness and the morphology of the printed foams. Airflow resistivity measurements of the closed-cell foams ( $R 10^6 \text{ Pa s/m}^2$ ) and open-cell foams ( $R 10^3$

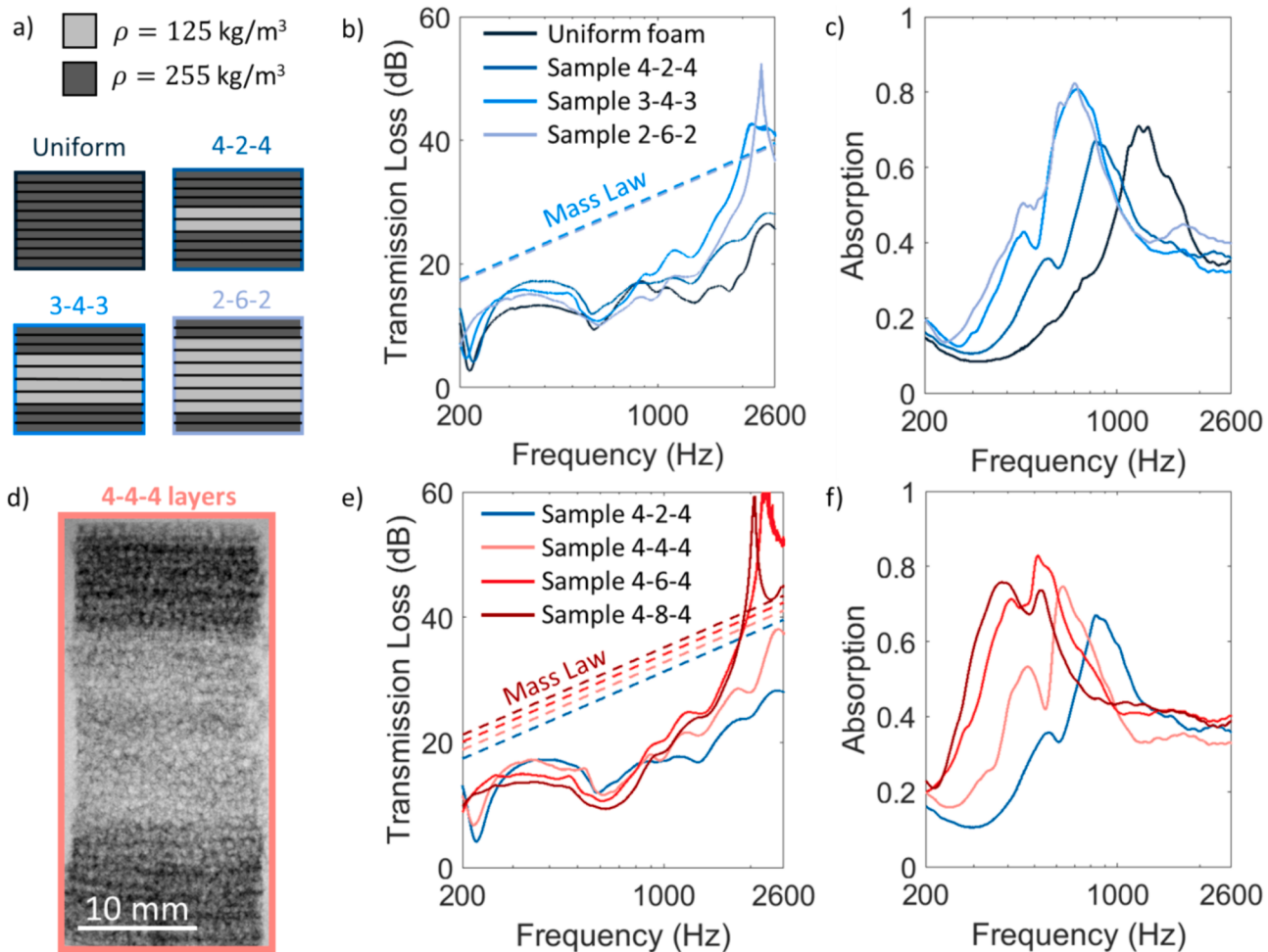


**Fig. 4.** Acoustic characterization of gradient foams with a low-density core. a) Schematic of tested foams with equal mass. The numbers refer to the number of layers with high density (dark) and low density (light). b) Measured transmission loss and c) Absorption of foams as a function of the frequency. d) Micro-CT visualization of 4-4-4 density gradient foam sample with stiff, soft, and stiff sections. e) Measured transmission loss and f) absorption of these foams as a function of the frequency. The dashed lines in b,e indicate the mass law.

Pa s/m<sup>2</sup>) are shown in Fig. SI 5, confirming the sharp transition between these morphologies.

The STL and absorption ( $\alpha$ ) were investigated for a range of 3D-printed foams with systematically varied properties. First, homogeneous foam samples ( $\rho = 150 \pm 10 \text{ kg/m}^3$ ) were printed with a thickness of  $5.4 \pm 0.4 \text{ mm}$ ,  $10.6 \pm 1.8 \text{ mm}$ , and  $20.7 \pm 0.8 \text{ mm}$  as shown in Fig. 3 (a). As shown in Fig. 3 (b, c), the STL of closed-cell foams ranged from < 5 dB at 200 Hz (all samples) to ~ 20 dB for the heaviest sample. For open-cell foams, the STL dramatically decreased, as interconnected pores enhance the sound transmission as compared to closed cells [45]. To place these measured results into perspective, the STL as expected for homogeneous rigid materials (the so-called 'mass-law'), was determined for each sample:

$$STL_{ML} = -10\log\left(1 + \left(\frac{2\pi\rho_f t f}{\rho c}\right)^2\right) \quad (9)$$

where  $\rho_f t$  is the surface mass density,  $\rho = 1.2 \text{ kg/m}^3$  is the density of air,  $t$  is the thickness of foam,  $f$  is the frequency of the impinging sound waves, and  $c = 343 \text{ m/s}$  is the speed of sound in air. One observes that the STL of the printed open-cell foams is negligible and that the closed-cell foams perform worse than ideal non-porous materials of homogeneous density. This is hardly surprising, as the inertia of a solid bulk material is sufficiently high to provide a barrier to the sound waves whereas the thin walls in porous materials may vibrate if exposed to sound waves. We will

first explore more results, before coming back to this topic in the discussion section. The measured absorption for closed- and open cell foams is shown in Fig. 3 (c). Here, the closed-cell foams exhibit clear peaks at frequencies between 1 kHz and 2 kHz. The absorption of open-cell samples surprisingly lower than the closed-cell foams, indicating that indeed the sound can propagate through the closed-cell foams via its thin cell walls.

Next, the STL and absorption were measured as a function of the foam density. Closed-cell samples with a thickness of 10 mm and densities of 202 and  $124 \text{ kg/m}^3$ , respectively, are shown in Fig. 3 (d, e). The maximum STL was observed for a density of  $150 \text{ kg/m}^3$  (Fig. 3 (f)). The sound absorption generally increased with decreasing density, as shown in Fig. 3 (g). For density  $\rho_f = 185 \text{ kg/m}^3$  (corresponding to  $P = 9.5 \text{ kPa}$ ), irregular formation of bubbles led to a different pore structure (Fig. SI 13), possibly explaining the shift to an absorption peak at higher frequency  $f > 2.6 \text{ kHz}$ . Average quantities of the STL characteristics for different thicknesses and densities are given in Table SI 2 and Table SI 3.

Sandwich-type foams were printed as a model system because these can be systematically controlled by the printing method. They may act as mass-spring-mass systems with enhanced dissipation in the central section, and thereby reduce the trade-off between STL and absorption.

Samples with a constant mass and different ratios of high-density and low-density sections were printed, as shown in Fig. 4 (a). The amount of stiff and soft layers of the printed samples is indicated by the numbering. For example, 4-2-4 indicates a sample consisting of 10 printed layers in

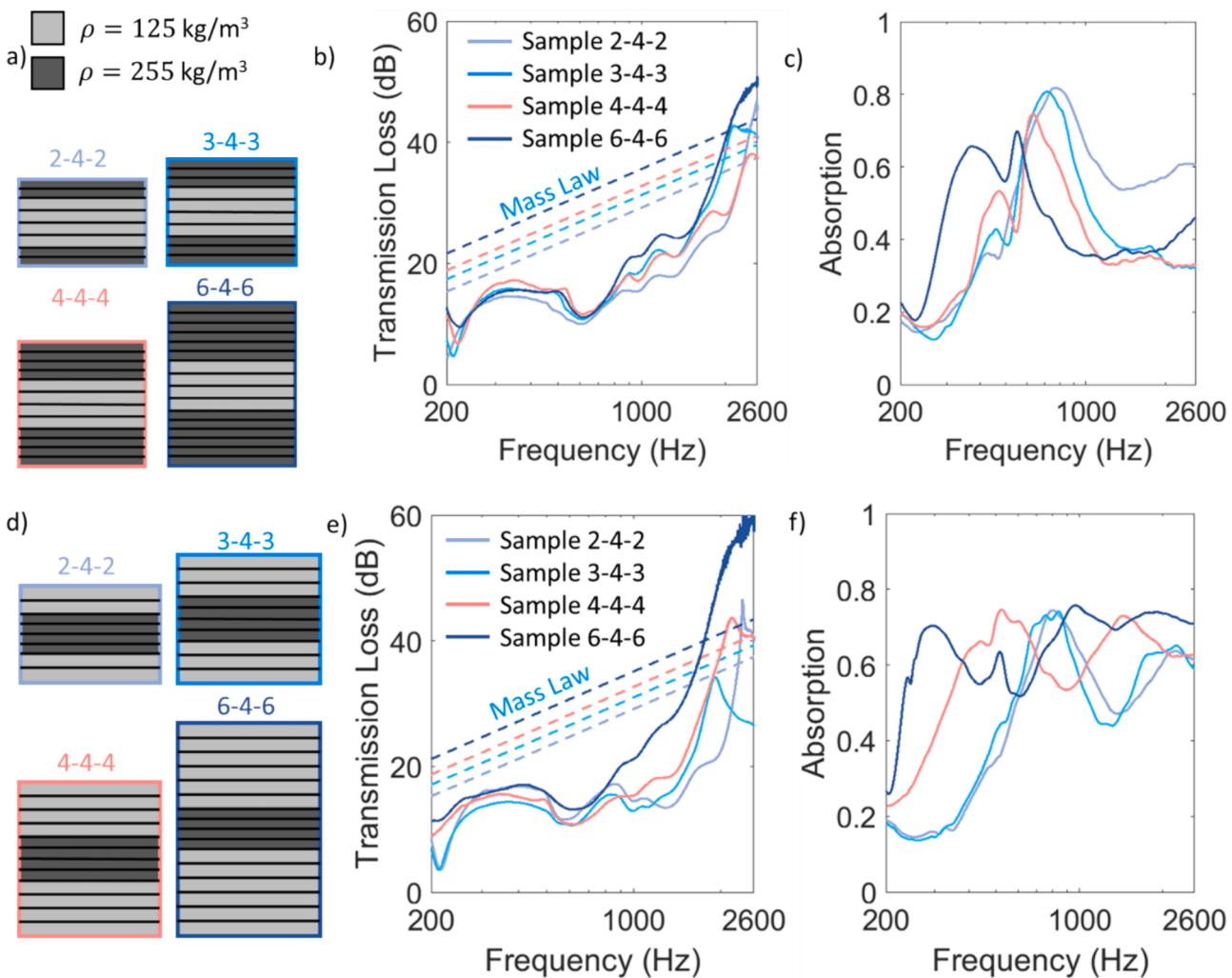


**Fig. 5.** Characterization of a-c) stiff-soft-stiff and d-f) soft-stiff-soft gradient foams. Schematic of tested foams with a) low-density sections and d) high density sections of increasing thickness. b) and e) Measured transmission loss and c) and f) Absorption coefficient of foams as a function of the frequency.

which two low-density layers are placed between two 4-layer dense sections at each side. For the denser samples (the uniform foam and the configuration 4–2–4) the STL increased for higher frequencies, and roughly lies  $10 \pm 5$  dB below the mass law as shown in Fig. 4 (b). For the samples with a thicker low-density core (3–4–3 and 2–6–2), clear peaks in the STL were observed at  $f \approx 2.3$  kHz, that exceed the mass law and locally result in a STL of  $\sim 50$  dB. The sandwich foams also slightly enhanced the STL as compared to uniform foams ( $< 5$  dB) for frequencies between 300 Hz and 500 Hz. The absorption of these samples is shown in Fig. 4 (c). Here, increasing the ratio of low-density to high-density foam led to a clear decrease of the main absorption frequency, which shifted from  $\sim 1250$  Hz to  $\sim 720$  Hz.

In a second set of measurements, we varied the thickness of the low-density core while the high-density end sections were kept constant. A Micro-CT image of a foam sample with 4–4–4 configuration is shown in Fig. 4 (d). The dense section appears darker due enhanced absorption of X-rays as compared to the low-density region. The STL of these samples is shown in Fig. 4 (e). For configurations 4–2–4, 4–4–4, 4–6–4, and 4–8–4, the measured average STL were 20 dB, 23.6 dB, 30.3 dB, and 27.8 dB, respectively. Remarkably, adding more mass resulted in a decrease of the overall STL in one case (sample 4–8–4), which is attributed especially to lower STL for frequencies  $300\text{Hz} < f < 1\text{kHz}$ . However, the samples with a thick low-density core resulted in very high peaks in the STL of  $\sim 60$  dB for frequencies around  $f = 2$  kHz.

The absorption peak of samples with a low-density core shifted to

values as low as  $f = 400$  Hz. These peaks were more broadband as compared to all samples discussed above, while maintaining reasonable absorption performance at higher frequencies. This broadening in absorption peaks was attributed to increased thickness of the foam samples.

Altogether from these results, the ability to tune low- or high-density center sections in graded foams enables control over the peak frequency and the acoustic performance. Especially thick low-density cores exhibit desirable properties for frequency-tunable STL and absorption (although at different frequencies). However, the peaks are still limited to a narrow bandwidth.

Finally, we evaluated the influence of the thickness of the high-density (stiff) outer section of gradient samples. Here, a low-density core section placed between high-density sandwiching layers was kept constant, as shown in Fig. 5 (a). The STL of the 2–4–2 design (8 layers) is higher than the 10-layer uniform foam with a higher mass as shown in Fig. 4 (a). However, all samples generally performed worse than the mass law as shown in Fig. 5 (b). With an increasing number of stiff layers, surface reflections were enhanced which improved the STL beyond 300 Hz. Increasing the thickness of the samples from 8 to 16 layers (2–4–2 to 6–4–6) also increased the interaction-driven dissipation and therefore the STL. The measured absorption of these samples is shown in Fig. 5 (c). The absorption peak decreased due to reflections and shifted to low frequencies if the high-density sections were increased in thickness.

**Fig. 5 (d, e, f)** shows the equivalent STL and absorption measurements for soft-stiff-soft gradient foams. Here, a high peak in the STL of 60 dB was observed for the thickest sample (6–4–6) at a frequency of 2600 Hz. The measured absorption was considerably enhanced as compared to the 2–4–2 foam sample and good absorption over a wider frequency range was observed, with high absorption ( $\alpha > 0.4$ ) down to 220 Hz. The high-absorption region also expanded in bandwidth, from 200 Hz to 2600 Hz for the 6–4–6 configuration. Therefore, significant dissipation-driven (maximum  $\sim 117\%$  increment) STL improvement was observed when the number of soft sandwiching layers was increased (**Fig. 5 (e)**).

Equivalent to **Fig. 4 (a, d)** and **Fig. 5 (a)**, measurements of the STL and absorption experiments were also performed for inverse configuration, i.e. soft-stiff-soft foams. In Fig. SI 9, gradient foams with constant mass and varying number of soft and stiff layers are evaluated. The STL and  $\alpha$  decreased with an increase of the thickness of the stiff core, and the absorption peak shifted from low to high frequencies. This trend is opposite to **Fig. 4 (c)**. The stiff-soft-stiff samples in **Fig. 4 (a, b, c)** outperformed the soft-stiff-soft samples (Fig. SI 9 (a, b, c)) in STL in line with the hypothesis that a mass-spring-mass system enhances the dissipation. However, soft-stiff-soft foams had higher and broader sound absorption than the stiff-soft-stiff foams.

The inverse configuration (soft-stiff-soft) of **Fig. 4 (d)** is shown in Fig. SI 9 (d) where the central stiff section was increased and layers constituting the soft sandwiching sections were held constant. The STL and sound absorption are shown as a function of the frequency in Fig. SI 9 (e, f). As compared to the stiff-soft-stiff configuration (**Fig. 4 (e, f)**), similar but less pronounced trends are observed.

In a final set of measurements, stiff and soft layers were simultaneously increased in thickness as shown in Fig. SI 10 and Fig. SI 11 for both stiff-soft-stiff and soft-stiff-soft configurations, respectively. Here, for gradient stiff-soft-stiff foams shown in Fig. SI 10 (a), the STL at frequencies above 600 Hz increased for the thicker, heavier samples as compared to the thinner samples, whereas only marginal changes were observed for lower frequencies (Fig. SI 10 (b, c)). Equivalent measurements of STL and sound absorption were done for the inverse configuration (soft-stiff-soft) in the gradient foams as shown in Fig. SI 11 (a, b, c). Table SI 4 summarizes the average STL, noise reduction coefficient (NRC), and average  $\alpha$  of the all the gradient sandwich configurations for comparison.

#### 4. Discussion

Homogeneous and gradient closed-cell foams generally provided a lower STL than the STL predicted by the mass law. A high airflow resistivity was confirmed, so that leaks in the material where sound can go through are an unlikely origin of this difference. Therefore, future work may aim for a different polymer that enhances visco-elastic damping within closed-cell foams. Materials that are more ecologically friendly (bio-sourced, bio-degradable, solvent-free, and vegan) are particularly attractive in this respect, as these would also resolve the long post-processing time required to dry our current foams and the creation of plastic parts. Recent acoustic foams that realize some of these goals incorporate recycled micro-plastics [46], organic PU foams [47], or polylactic acid (PLA) [26], and current efforts in our lab are geared towards this direction as well.

Gradient foams improved the STL as compared to homogeneous foams. Even minor gradients in the 2–2–2 stiff-soft-stiff foam absorbed sound over a wider band and with similar transmission loss performance as a high-density uniform foam consisting of 10 layers (Fig. SI 10 (a)). This would imply a  $\sim 40\%$  weight reduction. For the 6–4–6 sample with a low-density core, the STL reached 60 dB while broadband absorption ( $\alpha > 0.5$ ) was observed for frequencies above only 300 Hz. These results suggest that sandwich-inspired closed-cell gradient foams are effective dissipators at higher frequencies. Further optimization of the macroscopic properties (storage and loss moduli and effective density) and the

properties at cell level (cell size, wall thickness and material, local addition of dense particles, or controlled porosity to enhance viscous losses) are expected to provide further improvements of the printed foams. Finally, direct bubble writing also provides the option to create foams with 3D gradients, which might benefit dissipation of sound that impinges from multiple angles.

#### 5. Conclusion

Foam architectures with gradient densities were printed to assess their sound insulation and absorption. Using a recent method called “direct bubble writing”, the density of printed specimens was controlled by tuning the pressure of bubble generation during printing. A higher pressure (from 5.5 kPa to 8.5 kPa) decreased the density of the foams (from  $125 \text{ kg/m}^3$  to  $255 \text{ kg/m}^3$ ) as more gas was enclosed in the printed sample. The gas pressure was tuned during printing, between 5.5 kPa and 8.5 kPa, to create sandwich structures with stiff and soft sections, respectively. Foams with gradient designs provided broadband absorption ( $\alpha > 0.5$ ) above frequencies as low as 300 Hz, while enhancing the STL for frequencies above 1000 Hz as compared to uniform foams. The STL even reached peaks beyond 60 dB. This initial study proves that systematically tailoring the properties of gradient foams strongly enhances their acoustic properties as compared to homogeneous foams. Our foams do not yet outperform commercial foams, possibly because the polymer is not strictly visco-elastic. Future work may therefore focus on visco-elastic polymers that enhance dissipation, and thereby increase both the STL and the absorption.

#### CRediT authorship contribution statement

**Prasansha Rastogi:** Writing – original draft, Visualization, Software, Methodology, Investigation, Formal analysis, Conceptualization. **Cornelis H. Venner:** . **Claas Willem Visser:** Writing – review & editing, Visualization, Supervision, Methodology, Investigation, Conceptualization. **Ysbrand Wijnant:** Writing – review & editing, Visualization, Supervision, Software, Methodology, Investigation, Conceptualization.

#### Declaration of competing interest

The authors declare that they have no known competing financial interests or personal relationships that could have appeared to influence the work reported in this paper.

#### Data availability

Data will be made available on request.

#### Acknowledgements

The authors would like to acknowledge Dr. Shahrzad Ghaffari Mosanenzadeh for initial discussions and preliminary measurements, Dr. Yan Zhao and Dr. Mohammad Mehrali for the micro-CT scanning of the foam samples, Ing. P.J. van Swaaij (Andries) for the DMA operation, Ing. Z.A.J. Lok (Axel) for the impedance tube operation. Ing. Bob Siemerink, Steven Wanrooij, Ing. Walter Lette, Ing. H.F.G. Moed (Henk Jan), and Guanxing Kuang for their technical support in the lab and Dr. Olivier J. Nguon for the discussion.

#### Appendix A. Supplementary data

Supplementary data to this article can be found online at <https://doi.org/10.1016/j.apacoust.2024.110269>.

## References

- [1] Road Traffic in European Cities Exposes 60 Million People to Noise Levels Harmful to Health Available online: <https://www.isglobal.org/en/-/road-traffic-in-european-cities-exposes-60-million-people-to-noise-levels-harmful-to-health> (accessed on 1 June 2023).
- [2] European Environment Agency *Environmental Noise in Europe*, 2020.; 2020; ISBN 978-92-9480-209-5.
- [3] Noise Available online: <https://www.who.int/europe/news-room/fact-sheets/item/noise> (accessed on 1 June 2023).
- [4] Hadad O, Kröller-Schön S, Daiber A, Münzel T. The Cardiovascular Effects of Noise. *Dtsch Ärztebl Int* 2019. <https://doi.org/10.3238/arztebl.2019.0245>.
- [5] Martinez-Orozco JM, Barba A. Determination of insertion loss of noise barriers in spanish roads. *Appl Acoust* 2022;186:108435. <https://doi.org/10.1016/j.apacoust.2021.108435>.
- [6] Laxmi V, Thakre C, Vijay R. Evaluation of noise barriers based on geometries and materials: a review. *Environ Sci Pollut Res* 2022;29:1729–45. <https://doi.org/10.1007/s11356-021-16944-2>.
- [7] Trinh VH, Langlois V, Guilleminot J, Perrot C, Khidas Y, Pitois O. Tuning membrane content of sound absorbing cellular foams: fabrication, experimental evidence and multiscale numerical simulations. *Mater Des* 2019;162:345–61. <https://doi.org/10.1016/j.matdes.2018.11.023>.
- [8] Zhang C, Li J, Hu Z, Zhu F, Huang Y. Correlation between the acoustic and porous cell morphology of polyurethane foam: effect of interconnected porosity. *Mater Des* 2012;41:319–25. <https://doi.org/10.1016/j.matdes.2012.04.031>.
- [9] Statharas EC, Yao K, Rahimabady M, Mohamed AM, Tay FEH. Polyurethane/poly(vinylidene fluoride)/MWCNT composite foam for broadband airborne sound absorption. *J Appl Polym Sci* 2019;136:47868. <https://doi.org/10.1002/app.47868>.
- [10] Hasani Baferani A, Katbab AA, Ohadi AR. The role of sonication time upon acoustic wave absorption efficiency, microstructure, and viscoelastic behavior of flexible polyurethane/CNT nanocomposite foam. *Eur Polym J* 2017;90:383–91. <https://doi.org/10.1016/j.eurpolymj.2017.03.042>.
- [11] Choe H, Kim JH. Reactivity of isophorone diisocyanate in fabrications of polyurethane foams for improved acoustic and mechanical properties. *J Ind Eng Chem* 2019;69:153–60. <https://doi.org/10.1016/j.jiec.2018.09.025>.
- [12] Sailesh R, Yuvaraj L, Pitchaimani J, Doddamani M, Mailan Chinnapandi LB. Acoustic behaviour of 3D printed bio-degradable micro-perforated panels with varying perforation cross-sections. *Appl Acoust* 2021;174:107769. <https://doi.org/10.1016/j.apacoust.2020.107769>.
- [13] Hung T-C, Huang J-S, Wang Y-W, Lin K-Y. Inorganic polymeric foam as a sound absorbing and insulating material. *Constr Build Mater* 2014;50:328–34. <https://doi.org/10.1016/j.conbuildmat.2013.09.042>.
- [14] Yang Y, Chen Z, Xu T, Han R, Enefa Awuye D. Sound insulation and hydrophobic properties of phenolic resin modified melamine foam: role of micro-morphology. *Mater Res Express* 2019;6:075331. <https://doi.org/10.1088/2053-1591/ab17bb>.
- [15] Ji G, Xu J, Zhou J, Kang W. The exploration of transmission property by using the circular-interface types of porous acoustic metamaterials. *Int J Mech Sci* 2022;230:107558. <https://doi.org/10.1016/j.ijmecsci.2022.107558>.
- [16] Najib NN, Ariff ZM, Bakar AA, Sipaut CS. Correlation between the acoustic and dynamic mechanical properties of natural rubber foam: effect of foaming temperature. *Mater Des* 2011;32:505–11. <https://doi.org/10.1016/j.matdes.2010.08.030>.
- [17] Chen S, Jiang Y, Chen J, Wang D. The effects of various additive components on the sound absorption performances of polyurethane foams. *Adv Mater Sci Eng* 2015;2015:1–9. <https://doi.org/10.1155/2015/317561>.
- [18] Wang Y, Zhang C, Ren L, Ichchou M, Galland M-A, Bareille O. Influences of rice hull in polyurethane foam on its sound absorption characteristics. *Polym Compos* 2013;34:1847–55. <https://doi.org/10.1002/pc.22590>.
- [19] Chen S, Jiang Y. The acoustic property study of polyurethane foam with addition of bamboo leaves particles. *Polym Compos* 2018;39:1370–81. <https://doi.org/10.1002/pc.24078>.
- [20] Zhou D, Xiong Y, Yuan H, Shen Q, Luo G, Guo W. Enhanced sound insulation properties of microporous PMMA foams by constructing novel multilayered and directional cell structure (MDCS). *J Appl Polym Sci* 2020;137:49020. <https://doi.org/10.1002/app.49020>.
- [21] Kumar A, Gunasekaran V, Chinnapandi LBM, Pitchaimani J. Acoustic response behavior of porous 3D graphene foam plate. *Appl Acoust* 2020;169:107431. <https://doi.org/10.1016/j.apacoust.2020.107431>.
- [22] Kang YJ, Bolton JS. Sound transmission through elastic porous wedges and foam layers having spatially graded properties. *J Acoust Soc Am* 1997;102:3319–32. <https://doi.org/10.1121/1.419575>.
- [23] Tarkashvand A, Daneshjou K, Golmohammadi A. FG and viscoelastic models combination for vibroacoustic modeling of sandwich structures made of open and closed cell foam materials. *Compos Struct* 2021;259:113438. <https://doi.org/10.1016/j.compstruct.2020.113438>.
- [24] Xu Z, Zhang Z, Wang J, Chen X, Huang Q. Acoustic analysis of functionally graded porous graphene reinforced nanocomposite plates based on a simple quasi-3D
- HSDT. *Thin-Walled Struct* 2020;157:107151. <https://doi.org/10.1016/j.tws.2020.107151>.
- [25] Suethao, S.; Shah, D.U.; Smithipong, W. Recent Progress in Processing Functionally Graded Polymer Foams. *Materials* 2020, 13, 4060, doi: 10.3390/ma13184060.
- [26] Ghaffari Mosanenzadeh S, Naguib HE, Park CB, Atalla N. Design and development of novel bio-based functionally graded foams for enhanced acoustic capabilities. *J Mater Sci* 2015;50:1248–56. <https://doi.org/10.1007/s10853-014-8681-6>.
- [27] Costantini M, Jaroszewicz J, Kozoń Ł, Szlazak K, Święzakowski W, Garstecki P, et al. 3D-printing of functionally graded porous materials using on-demand reconfigurable microfluidics. *Angew Chem Int Ed* 2019;58:7620–5. <https://doi.org/10.1002/anie.201900530>.
- [28] Danielsson M, Grenestedt JL. Gradient foam core materials for sandwich structures: preparation and characterisation. *Compos Part Appl Sci Manuf* 1998;29:981–8. [https://doi.org/10.1016/S1359-835X\(97\)00058-4](https://doi.org/10.1016/S1359-835X(97)00058-4).
- [29] Matijasevic B, Banhart J. Improvement of aluminium foam technology by tailoring of blowing agent. *Scr Mater* 2006;54:503–8. <https://doi.org/10.1016/j.scriptamat.2005.10.045>.
- [30] Lobos J, Thirumuruganandham SP, Rodríguez-Pérez MA. Density gradients, cellular structure and thermal conductivity of high-density polyethylene foams by different amounts of chemical blowing agent. *Polymers* 2022;14:4082. <https://doi.org/10.3390/polym14194082>.
- [31] Jahani D, Ameli A, Jung PU, Barzegari MR, Park CB, Naguib H. Open-cell cavity-integrated injection-molded acoustic polypropylene foams. *Mater Des* 2014;53:20–8. <https://doi.org/10.1016/j.matdes.2013.06.063>.
- [32] Ciocich A, Kennedy J, Leiba R, Flanagan L, Culleton M. The impact of surface roughness on an additively manufactured acoustic material: an experimental and numerical investigation. *J Sound Vib* 2023;546:117434. <https://doi.org/10.1016/j.jsv.2022.117434>.
- [33] Visser CW, Amato DN, Mueller J, Lewis JA. Architected polymer foams via direct bubble writing. *Adv Mater* 2019;31:1904668. <https://doi.org/10.1002/adma.201904668>.
- [34] Rastogi P, Venner CH, Visser CW. Deposition offset of printed foam strands in direct bubble writing. *Polymers* 2022;14:2895. <https://doi.org/10.3390/polym14142895>.
- [35] Amato DN, Amato DV, Sandoz M, Weigand J, Patton DL, Visser CW. Programmable porous polymers via direct bubble writing with surfactant-free inks. *ACS Appl Mater Interfaces* 2020;12:42048–55. <https://doi.org/10.1021/acsmami.0c07945>.
- [36] Maiti A, Small W, Lewicki JP, Weisgraber TH, Duoss EB, Chinn SC, et al. 3D printed cellular solid outperforms traditional stochastic foam in long-term mechanical response. *Sci Rep* 2016;6:24871. <https://doi.org/10.1038/srep24871>.
- [37] Lee TY, Guymon CA, Jönsson ES, Hoyle CE. The effect of monomer structure on oxygen inhibition of (Meth)acrylates photopolymerization. *Polymer* 2004;45:6155–62. <https://doi.org/10.1016/j.polymer.2004.06.060>.
- [38] Burford RJ, Fryzuk MD. Examining the relationship between coordination mode and reactivity of dinitrogen. *Nat Rev Chem* 2017;1:0026. <https://doi.org/10.1038/s41570-017-0026>.
- [39] Krongauz VV, Schmelzer ER. Oxygen effects on anisotropic photopolymerization in polymer matrices. *Polymer* 1992;33:1893–901. [https://doi.org/10.1016/0032-3861\(92\)90489-J](https://doi.org/10.1016/0032-3861(92)90489-J).
- [40] Vitale A, Bongiovanni R, Ameduri B. Fluorinated oligomers and polymers in photopolymerization. *Chem Rev* 2015;115:8835–66. <https://doi.org/10.1021/cr500120>.
- [41] O'Brien AK, Bowman CN. Impact of oxygen on photopolymerization kinetics and polymer structure. *Macromolecules* 2006;39:2501–6. <https://doi.org/10.1021/ma0518631>.
- [42] Scherzer T. UV-induced photopolymerization of acrylates. *Macromol Chem Phys* 2012;213:324–34. <https://doi.org/10.1002/macp.201100485>.
- [43] Wang Y, Ma H, Xie K, Fu T, Chen J, Liu Y. Nonlinear bending of a sandwich beam with metal foam and GPLRC face-sheets using chebyshev-Ritz method: effects of agglomeration and internal pore. *Thin-Walled Struct* 2022;181:110035. <https://doi.org/10.1016/j.tws.2022.110035>.
- [44] Chai HW, Li HY, Xiao XH, Huang JY, Luo SN. Correlation between cell wall buckling and deformation banding in a closed-cell foam. *Scr Mater* 2019;170:177–82. <https://doi.org/10.1016/j.scriptamat.2019.06.006>.
- [45] Ji Y, Chen S, Cheng Y. Synthesis and acoustic study of a new tung oil-based polyurethane composite foam with the addition of miscanthus lutarioriparius. *Polymers* 2019;11:1144. <https://doi.org/10.3390/polym111144>.
- [46] Caniato M, Cozzarini L, Schmid C, Gasparella A. Acoustic and thermal characterization of a novel sustainable material incorporating recycled microplastic waste. *Sustain Mater Technol* 2021;28:e00274.
- [47] Selvaraj VK, Subramanian J, Gupta M, Gayen M, Mailan Chinnapandi LB. An experimental investigation on acoustical properties of organic PU foam reinforced with nanoparticles fabricated by hydrothermal reduction technique to emerging applications. *J Inst Eng India Ser D* 2020;101:271–84. <https://doi.org/10.1007/s40033-020-00238-x>.